

Microscopic pairing fingerprint of the iron-based superconductor $\text{Ba}_{1-x}\text{K}_x\text{Fe}_2\text{As}_2$

T. Böhm,^{1,2,3} F. Kretzschmar,^{1,2,*} A. Baum,^{1,2} M. Rehm,^{1,2,†} D. Jost,^{1,2} R. Hosseinian Ahangharnejhad,^{1,2,‡}
R. Thomale,⁴ C. Platt,⁵ T. A. Maier,⁶ W. Hanke,⁴ B. Moritz,³ T. P. Devereaux,^{3,7} D. J. Scalapino,⁸
S. Maiti,⁹ P. J. Hirschfeld,⁹ P. Adelman,¹⁰ T. Wolf,¹⁰ Hai-Hu Wen,¹¹ and R. Hackl¹

¹Walther Meissner Institut, Bayerische Akademie der Wissenschaften, 85748 Garching, Germany

²Fakultät für Physik E23, Technische Universität München, 85748 Garching, Germany

³Stanford Institute for Materials and Energy Sciences, SLAC National Accelerator Laboratory,
2575 Sand Hill Road, Menlo Park, California 94025, USA

⁴Theoretical Physics, University of Würzburg, 97074 Würzburg, Germany

⁵Department of Physics, McCullough Building, Stanford University, Stanford, California 94305-4045, USA

⁶Center for Nanophase Materials Sciences and Computer Science and Mathematics Division,
Oak Ridge National Laboratory, Oak Ridge, Tennessee 37831-6494, USA

⁷Geballe Laboratory for Advanced Materials, Stanford University, Stanford, CA 94305, USA

⁸Physics Department, University of California, Santa Barbara, California 93106-9530, USA

⁹Department of Physics, University of Florida, Gainesville, Florida 32611, USA

¹⁰Karlsruher Institut für Technologie, Institut für Festkörperphysik, 76021 Karlsruhe, Germany

¹¹National Laboratory of Solid State Microstructures and Department of Physics, Nanjing University, Nanjing 210093, China
(Dated: June 18, 2021)

Resolving the microscopic pairing mechanism and its experimental identification in unconventional superconductors is among the most vexing problems of contemporary condensed matter physics. We show that Raman spectroscopy provides an avenue for this quest by probing the structure of the pairing interaction at play in an unconventional superconductor. As we study the spectra of the prototypical Fe-based superconductor $\text{Ba}_{1-x}\text{K}_x\text{Fe}_2\text{As}_2$ for $0.22 \leq x \leq 0.70$ in all symmetry channels, Raman spectroscopy allows us to distill the leading s -wave state. In addition, the spectra collected in the B_{1g} symmetry channel reveal the existence of two collective modes which are indicative of the presence of two competing, yet sub-dominant, pairing tendencies of $d_{x^2-y^2}$ symmetry type. A comprehensive functional Renormalization Group (fRG) and random-phase approximation (RPA) study on this compound confirms the presence of the two sub-leading channels, and consistently matches the experimental doping dependence of the related modes. The synopsis of experimental evidence and theoretical modelling supports a spin-fluctuation mediated superconducting pairing mechanism.

PACS numbers: 74.20.Mn, 74.20.Rp, 74.70.Xa, 74.25.nd

I. MICROSCOPIC PAIRING

In superconductors such as the cuprates, ferro-pnictides, ruthenates or heavy-fermion systems, the pairing mechanism is believed to be unconventional and related to direct electronic interactions rather than conventional electron-phonon mediated couplings. Yet, the precise microscopic mechanism, the “glue” that binds electrons into Cooper pairs, remains elusive. Measurements of the superconducting ground state alone are insufficient to unambiguously determine whether a superconductor has a conventional or unconventional pairing mechanism. Raman spectroscopy provides the avenue for gathering the missing information in *both dominant and sub-dominant* pairing channels.

In comparison to other techniques, Raman spectroscopy (which involves inelastic scattering of light) is rather unique as it provides access to both the energy gaps of a superconductor and to bound states inside the gaps² that serve as signposts marking the strength of a given pairing interaction.

These bound states were predicted a long time ago by Bardasis and Schrieffer (BS)³ and are collective excitations that correspond to the phase oscillations of

the ground state order parameter triggered by the sub-dominant (d -wave) interactions. The BS modes or particle-particle excitons couple to the Raman probe, but there is no consensus yet about their observation in conventional superconductors^{4,5}. Fe-based superconductors (FeSCs), however, presented a more favorable scenario to search for this physics as many of them are believed to exhibit s_{\pm} pairing (with an order parameter that may change sign between Fermi surface pockets^{6–10}) and also a sub-leading d -wave pairing interaction that can be strongly competitive. Theoretical calculations based on spin fluctuations have even argued that d -wave could become the ground state for sufficiently strong hole-doping^{11,12}.

As a result, Scalapino and Devereaux¹³ performed a ‘bare-bones’ calculation for a typical FeSC electronic structure with s_{\pm} symmetry of the ground state and anisotropic gaps, showing that the mode frequency should depend on $1/\lambda_d - 1/\lambda_s$, where λ_d and λ_s are the respective coupling strengths of the electrons to the glue that binds the Cooper pair in the d -wave and the s -wave channel. Recent measurements on $\text{Ba}_{1-x}\text{K}_x\text{Fe}_2\text{As}_2$ ^{5,14,15}, $\text{NaFe}_{1-x}\text{Co}_x\text{As}$ ¹⁶, $\text{Ba}(\text{Fe}_{1-x}\text{Co}_x)_2\text{As}_2$ ^{17,18} found peaks in the B_{1g} spectrum

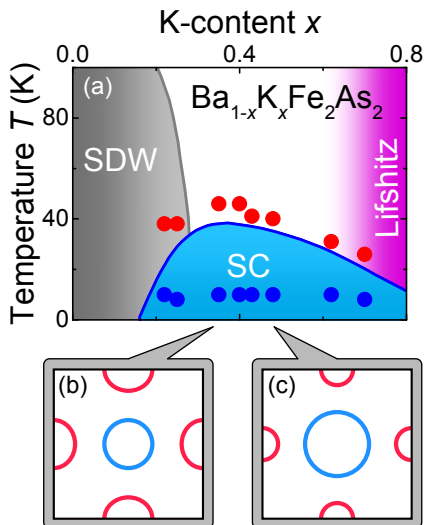


FIG. 1. Phase diagram and schematics of doping dependent Fermi surfaces in $\text{Ba}_{1-x}\text{K}_x\text{Fe}_2\text{As}_2$. (a) The sampling points of the measurements are compiled in the phase diagram¹ as blue and red dots deep in the superconducting state and slightly above T_c , respectively. (b) and (c) Schematic Brillouin zone and Fermi surface in the 1 Fe unit cell. With increasing hole-doping x the hole pockets (blue) grow and the electron pockets (red) shrink (changes exaggerated).

which were consistent with a collective mode, but its direct association with a BS mode was unclear.

In this work, we confirm the presence of two sub-dominant pairing interactions, as predicted theoretically, by providing an ubiquitous identification of *multiple* BS modes in the B_{1g} spectrum of the prototypical ferro-pnictide $\text{Ba}_{1-x}\text{K}_x\text{Fe}_2\text{As}_2$ (BKFA). Each sub-dominant pairing interaction results in a BS mode¹⁹. This perspective underlies our identification of the two new peaks in the Raman spectrum with B_{1g} BS modes. The analysis of our experimental peak energies also supports this scenario and even allows us to empirically extract the relative coupling strengths $\lambda_{d(1)}/\lambda_s, \lambda_{d(2)}/\lambda_s$, of the two distinct B_{1g} ($d_{x^2-y^2}$) pairing channels competing with the s_{\pm} ground state. We could reproduce the presence of all three pairing channels by performing a functional Renormalization Group (fRG) as well as a Random Phase Approximation (RPA) study. Since the fRG calculation includes the leading fluctuations (magnetic, superconducting, charge density wave etc.) whereas the RPA is distinctly based on magnetically driven (i.e. spin-fluctuation-induced) pairing, the agreement of both approaches with each other and the experiment strongly points to a spin-fluctuation scenario in BKFA. Since a direct observation of spin fluctuations below T_c is not achievable by Raman scattering (the relevant scattering states are gapped out) we study the BS modes which remain as the fingerprints of the microscopic pairing interactions.

II. RESULTS

To this end we measured eight samples of BKFA in the wide doping range $0.22 \leq x \leq 0.70$ as indicated in Fig. 1 (a) and described in detail in Ref. 20. BKFA forms high quality single crystals^{21–23} and fairly clean and isotropic gaps^{24,25}. In the samples with $x = 0.22$ and $x = 0.25$ superconductivity and the spin density wave (SDW) state coexist. The samples with $x = 0.62$ and $x = 0.70$ are close to a putative Lifshitz transition at $x \sim 0.8$ ²⁶. To present the case for the physics of sub-dominant pairing interactions, we wish to stay away from special effects arising from magnetism or disappearance of pockets and focus on the samples with $x = 0.35, 0.40, 0.43, 0.48$. In this range, the Raman spectra in the B_{1g} symmetry channel (1 Fe unit cell) change continuously as shown in Fig. 2 (a–d). Spectra of the other symmetries and outside the range $0.35 \leq x \leq 0.48$ are compiled in Ref. 20.

The spectra above the superconducting transition temperature T_c are dominated by the electron-hole continua. Below T_c additional (symmetry-dependent) structures appear in the energy range up to approximately 300 cm^{-1} , and the spectral weight is redistributed from below twice the superconducting gap 2Δ to energies above. New features arise from pair breaking, excitations across the gap, and exciton-like bound states^{2,5,19}. With increasing doping and a concomitant reduction of T_c , the peaks move to lower energies.

To illustrate why BKFA is a model superconductor for investigating BS modes we highlight the changes in the electronic spectra below T_c . For this purpose we subtract the normal state response from the superconducting spectra. This procedure eliminates temperature-independent components of the spectra like the A_{2g} response and phonons in the symmetries A_{1g} and B_{2g} ²⁰. By plotting the difference $\Delta R\chi''(\tilde{\Omega}) \equiv R\chi''(\tilde{\Omega}, T = 10 \text{ K}) - R\chi''(\tilde{\Omega}, T \gtrsim T_c)$ in Fig. 2 (e) with $\tilde{\Omega} = \hbar\Omega/k_B T_c$ we extract superconductivity-induced features of pure B_{1g} symmetry. Due to the full gap, the difference spectra become negative at low energies and three pronounced peaks are observed. The differences between normal and superconducting spectra disappear ($\Delta R\chi'' \rightarrow 0$) close to $\tilde{\Omega} = 8$. The highest peak [purple arrows in Fig. 2 (e)] at approximately 6.2, which we identify with the maximal gap, depends weakly on doping. The range of $2\Delta/k_B T_c \simeq 6.2$ is in qualitative agreement with the results from other methods^{24,25,27}. This enables us to check the validity of the RPA and fRG approaches in a coupled system of intermediate strength. There are two additional narrow lines in the ranges 1.5–3 (green arrows) and 4–5.5 (orange arrows) displaying a strong monotonic downshift with increasing K content.

At optimal doping ($x = 0.40$), evidence was furnished that the narrow line at 5.3 [140 cm^{-1} in Fig. 2 (b)] results from a bound state of two electrons of a broken Cooper pair⁵. The other narrow line at 2.8 [75 cm^{-1}

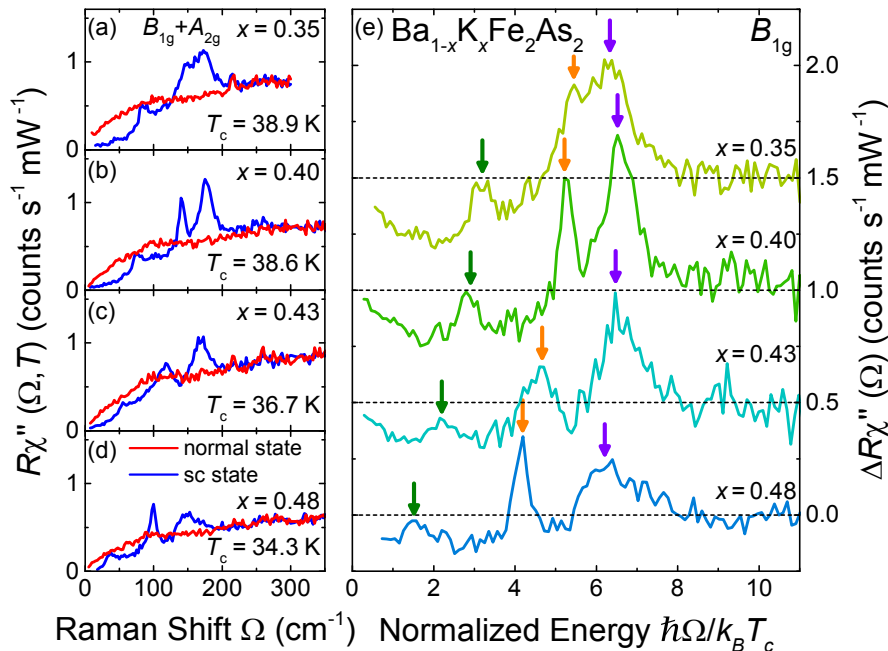


FIG. 2. Doping dependence of the Raman spectra in B_{1g} symmetry. (a-d) Raman response $R\chi''(\Omega, T, x)$ (raw data after division by the Bose-Einstein factor) of $\text{Ba}_{1-x}\text{K}_x\text{Fe}_2\text{As}_2$ in B_{1g} symmetry above (red) and below (blue) T_c close to optimal doping in the range $x = 0.35$ to $x = 0.48$. (e) Difference spectra $\Delta R\chi''(\Omega, x)$ in B_{1g} symmetry. The energy scale is normalized to the respective T_c values of the differently doped samples. The intensities are off-set, the dashed horizontal lines mark zero. The purple arrows indicate the pair-breaking features at high energy. Green and orange arrows mark two BS modes pulled off the energy gap. They correspond to the sub-dominant channels $d(1)$ and $d(2)$, respectively.

in Fig. 2(b)] is difficult to properly assign on the basis of just one doping level. A suggestion for this peak as a second, smaller pair-breaking peak and a single BS mode at 5.3 was given in e.g. Ref. 5. However, upon studying several doping levels and all symmetries²⁰ we find the following systematics in favor of two BS modes: (i) The two in-gap modes appear only in B_{1g} symmetry. (ii) As opposed to the pair-breaking maxima at approximately $6 k_B T_c$ there are no other gap energies observed the two sharp modes could correspond to. (iii) Upon doping K for Ba the in-gap modes increasingly split off of the pair-breaking maximum. The nearly identical doping dependences of the two modes and the absence of pair-breaking features in other symmetries suggest that both modes are linked to the maximal gap. The unique appearance of narrow BS modes in B_{1g} symmetry for $0.35 \leq x \leq 0.48$ indicates that there are sub-dominant interactions with d -wave symmetry. We label the corresponding sub-leading B_{1g} channels as $d(1)$ and $d(2)$ for the lower- and the higher-energy line, respectively.

In Fig. 3(a) we compile experimental peak energies derived from Fig. 2. The difference between 2Δ (purple) and the BS modes in the range $1.5 - 5 k_B T_c$ (green and orange) corresponds to the binding energies $E_{b(i)} = 2\Delta - \Omega_{\text{BS}(i)}$ with $i = 1, 2$ of the bound states. The ratios of the relative coupling strengths $\lambda_{d(i)}/\lambda_s$ are estimated from $E_{b(i)}/2\Delta$ using the results of Refs. 4, 5, and 13 and $\lambda_s = 0.7$ from Refs. 28 and 29. Note that we used a

doping-independent value of 0.7 for this estimate as the ratios $\lambda_{d(i)}/\lambda_s$ are weakly sensitive to small changes of λ_s ²⁰.

III. THEORETICAL METHODS

According to Ref. 19, the presence of two BS modes in the same symmetry channel must imply the presence of two pairing interactions with different form factors competing with the ground state. Thus in addition to the ratios $\lambda_{d(i)}/\lambda_s$ derived from experiment, we show in Fig. 3(b) and (c) the results of two microscopic studies using fRG and RPA schemes that precisely identify these pairing channels and also provide an estimate for $\lambda_{d(i)}/\lambda_s$. The comparison of the two independent approaches allows us to pin down the origin of the leading pairing channel since the fRG includes all interactions^{30,31} whereas the RPA focuses on the spin sector as spelled out in detail in Ref. 20. Another difference becomes apparent in the procedure used to determine the effective interaction potential. The fRG analysis is designed to start its unbiased renormalization group flow already at energies above the bandwidth while the effective model scale entering the RPA resummation has to be chosen at comparably lower energies²⁰. As it turns out, however, in spite of these differing initializations, transcending further down to energies at which supercon-

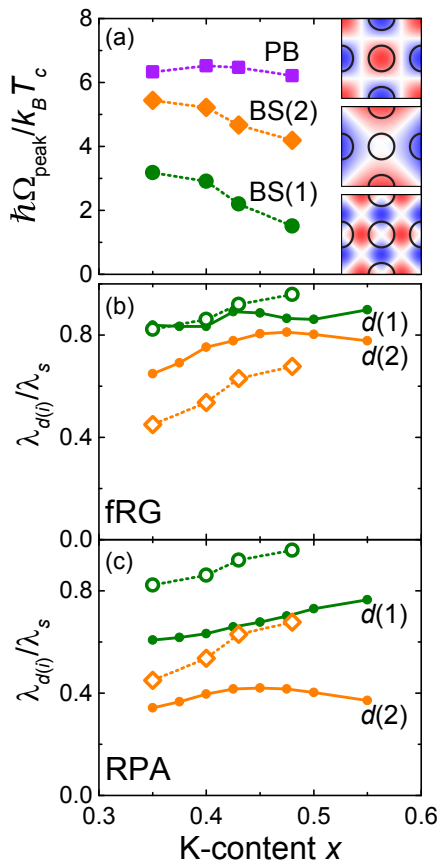


FIG. 3. Gap energies and relative coupling strengths. (a) Doping dependence of the characteristic B_{1g} gap energies. The highest pair-breaking energy Ω_{PB} scales approximately with T_c . The maxima at $\Omega_{\text{BS}(1)}$ and $\Omega_{\text{BS}(2)}$ inside the gap decrease faster than T_c . (b) and (c) Relative coupling parameters of the sub-dominant ($\lambda_{d(i)}$) and the dominant (λ_s) channel. With a dominant interaction of $\lambda_s = 0.7^{28,29}$, the ratios for $\lambda_{d(i)}/\lambda_s$ are extracted from the experiment (open green and orange symbols, corresponding to $d(1)$ and $d(2)$, respectively). The green and orange dots represent results from fRG and RPA¹⁹ calculations in panels (b) and (c), respectively.

ductivity occurs yields similar findings for both methods.

In order to determine the hierarchy of pairing interactions from the effective pairing vertex V from either fRG or RPA, we decompose this pairing channel into eigenmodes, which is tantamount to solving an eigenvalue problem of the form²⁰

$$\int_{\text{FS}} dq V(k, q) g_\alpha(q) = \lambda_\alpha g_\alpha(k), \quad (1)$$

where k comprises momentum, band, and spin degrees of freedom, and α is the index consecutively numbering the different eigenvalues. We assume α to be ordered according to the magnitude of eigenvalues λ_α . $g_\alpha(k)$ is the pairing eigenvector along the the Fermi surfaces specifying the symmetry of the pairing.

From both fRG and RPA, we find $\lambda_s, g_s(k)$ ($\alpha = 1$)

to be the dominant superconducting pairing of A_{1g} (s_\pm) type and $\lambda_{d(1,2)}, g_{d(1,2)}(k)$ ($\alpha = 2, 3$) the sub-leading B_{1g} type couplings. Schematic eigenvectors $g_\alpha(\mathbf{k})$ for $\alpha = 1, 2, 3$ are shown as insets in Fig. 3(a). These results apply to both $V \equiv V_{\text{fRG}}^\Lambda$ and $V \equiv V_{\text{RPA}}$ when used in Eq. (1), where Λ is the low-energy cutoff in the fRG flow that serves as an upper bound for the transition temperature^{20,30,31}. The leading eigenvalue $\lambda_s \equiv \lambda_1$ in Eq. (1), which is a function of Λ in the case of fRG, then determines the leading Fermi surface instability. The ratios of the eigenvalues $\lambda_{d(1,2)}/\lambda_s \equiv \lambda_{2,3}/\lambda_1$ determine the peak positions of the BS modes and are shown along with the experiments in Fig. 3(b) and (c). Note that $\lambda_2 \equiv \lambda_{d1}$ fits the extended d -wave harmonic form predicted in Ref. 11.

IV. CONCLUSIONS

From the plethora of theories intended to describe the iron-based superconductors, the comparison with the experiment now enables us, as a first step, to verify the validity of fRG and RPA for the intermediately coupled electronic system of BKFA. We find in accordance with the experiment that both approaches predict the strongest sub-leading channels to be of d -wave symmetry. Furthermore, the theoretical predictions for the relative coupling parameters as shown in Fig. 3 are in good agreement with the experiment. The fRG results are in quantitative agreement, the RPA values systematically underestimate the relative coupling strength but are still close to the experiment. Hence we conclude that fRG and RPA are suitable to describe the experiment around optimal doping, $0.35 \leq x \leq 0.48$, where the two collective BS modes can be identified. Besides the agreement with the experiment the fRG interaction eigenvectors $g_\alpha(\mathbf{k})$ match very well with those obtained from the spin-fluctuation-based RPA analysis in all three channels ($\alpha = 1, 2, 3$). These agreements indicate that spin fluctuations are an important if not the leading interaction in the system under consideration.

The results presented here put narrow constraints on the description of the Raman data and render differing interpretations^{16,18} rather unlikely to be applicable to BKFA. Hence, the observation of two collective modes inside the gap of a superconductor establishes a novelty in terms of experimental analysis which promises to have an impact on the general understanding of unconventional superconductivity. Along with the magnitude of the gap, the modes reveal the hierarchy of pairing states in a prototypical material, in full agreement with microscopic predictions. As a result, our experiment demonstrates the unique possibilities of using light scattering as a probe for observing unconventional pairing fingerprints.

ACKNOWLEDGMENTS

We acknowledge useful discussions with L. Benfatto, A. Eberlein, D. Einzel, S. A. Kivelson, C. Meingast, and I. Tüttő. W.H. gratefully acknowledges the hospitality of the Institute for Theoretical Physics at the University of California Santa Barbara. Financial support for the work came from the Deutsche Forschungsgemeinschaft (DFG) via the Priority Program SPP 1458 (T.B., A.B., R.H., C.P. and W.H., project nos. HA 2071/7-2 and HA 1537/24-2), the Collaborative Research Centers SFB 1170 (W.H., C.P., and R.T.) and TRR 80 (F.K. and R.H.), the Bavarian Californian Technology Center BaCaTeC (T.B. and R.H., project no. A5[2012-

2]), the European Research Council (ERC) through ERC-StG-Thomale-TOPOLECTRICS (R.T.), and from the U.S. Department of Energy (DOE), Office of Basic Energy Sciences (B.M. and T.P.D.), Division of Materials Sciences and Engineering, under Contract No. DEAC02-76SF00515. The RPA calculations were conducted at the Center for Nanophase Materials Sciences, which is a DOE Office of Science User Facility. The work in China (H.-H.W.) was supported by the National Key Research and Development Program of China (2016YFA0300401), and the National Natural Science Foundation of China (NSFC) via projects A0402/11534005 and A0402/11374144.

-
- * Present address: Intel Mobile Communications, Am Campeon 10-12, 85579 Neubiberg, Germany
- † Present address: Schreinerei Kugler, Augsburg Str. 6, 86633 Neuburg, Germany
- ‡ Present address: School of Solar and Advanced Renewable Energy, University of Toledo, Toledo, Ohio 43606, USA
- ¹ A. E. Böhmer, P. Burger, F. Hardy, T. Wolf, P. Schweiss, R. Fromknecht, M. Reinecker, W. Schranz, and C. Meingast, *Phys. Rev. Lett.* **112**, 047001 (2014).
 - ² T. P. Devereaux and R. Hackl, *Rev. Mod. Phys.* **79**, 175 (2007).
 - ³ A. Bardasis and J. R. Schrieffer, *Phys. Rev.* **121**, 1050 (1961).
 - ⁴ H. Monien and A. Zawadowski, *Phys. Rev. B* **41**, 8798 (1990).
 - ⁵ T. Böhm, A. F. Kemper, B. Moritz, F. Kretzschmar, B. Muschler, H.-M. Eiter, R. Hackl, T. P. Devereaux, D. J. Scalapino, and H.-H. Wen, *Phys. Rev. X* **4**, 041046 (2014).
 - ⁶ I. I. Mazin, D. J. Singh, M. D. Johannes, and M. H. Du, *Phys. Rev. Lett.* **101**, 057003 (2008).
 - ⁷ R. Yu, Q. Si, P. Goswami, and E. Abrahams, *Journal of Physics: Conference Series* **449**, 012025 (2013).
 - ⁸ H. Hosono and K. Kuroki, *Physica C: Superconductivity and its Applications* **514**, 399 (2015), superconducting Materials: Conventional, Unconventional and Undetermined.
 - ⁹ A. V. Chubukov, R. M. Fernandes, and J. Schmalian, *Phys. Rev. B* **91**, 201105 (2015).
 - ¹⁰ P. J. Hirschfeld, *C. R. Physique* **17**, 197 (2016), iron-based superconductors / Supraconducteurs base de fer.
 - ¹¹ R. Thomale, C. Platt, J. Hu, C. Honerkamp, and B. A. Bernevig, *Phys. Rev. B* **80**, 180505 (2009).
 - ¹² R. Thomale, C. Platt, W. Hanke, J. Hu, and B. A. Bernevig, *Phys. Rev. Lett.* **107**, 117001 (2011).
 - ¹³ D. J. Scalapino and T. P. Devereaux, *Phys. Rev. B* **80**, 140512 (2009).
 - ¹⁴ F. Kretzschmar, B. Muschler, T. Böhm, A. Baum, R. Hackl, H.-H. Wen, V. Tsurkan, J. Deisenhofer, and A. Loidl, *Phys. Rev. Lett.* **110**, 187002 (2013).
 - ¹⁵ S.-F. Wu, P. Richard, H. Ding, H.-H. Wen, G. Tan, M. Wang, C. Zhang, P. Dai, and G. Blumberg, *Phys. Rev. B* **95**, 085125 (2017).
 - ¹⁶ V. K. Thorsmølle, M. Khodas, Z. P. Yin, C. Zhang, S. V. Carr, P. Dai, and G. Blumberg, *Phys. Rev. B* **93**, 054515 (2016).
 - ¹⁷ B. Muschler, W. Prestel, R. Hackl, T. P. Devereaux, J. G. Analytis, J.-H. Chu, and I. R. Fisher, *Phys. Rev. B* **80**, 180510 (2009).
 - ¹⁸ Y. Gallais, I. Paul, L. Chauvière, and J. Schmalian, *Phys. Rev. Lett.* **116**, 017001 (2016).
 - ¹⁹ S. Maiti, T. A. Maier, T. Böhm, R. Hackl, and P. J. Hirschfeld, *Phys. Rev. Lett.* **117**, 257001 (2016).
 - ²⁰ For details see Appendix.
 - ²¹ M. Rotter, M. Tegel, and D. Johrendt, *Phys. Rev. Lett.* **101**, 107006 (2008).
 - ²² B. Shen, H. Yang, Z.-S. Wang, F. Han, B. Zeng, L. Shan, R. Cong, and H.-H. Wen, *Phys. Rev. B* **84**, 184512 (2011).
 - ²³ A. E. Karkin, T. Wolf, and B. N. Goshchitskii, *J. Phys.: Condens. Matter* **26**, 275702 (2014).
 - ²⁴ D. V. Evtushinsky, D. S. Inosov, V. B. Zabolotnyy, A. Koitzsch, M. Knupfer, B. Büchner, M. S. Viazovska, G. L. Sun, V. Hinkov, A. V. Boris, C. T. Lin, B. Keimer, A. Varykhalov, A. A. Kordyuk, and S. V. Borisenko, *Phys. Rev. B* **79**, 054517 (2009).
 - ²⁵ K. Nakayama, T. Sato, P. Richard, Y.-M. Xu, T. Kawahara, K. Umezawa, T. Qian, M. Neupane, G. F. Chen, H. Ding, and T. Takahashi, *Phys. Rev. B* **83**, 020501 (2011).
 - ²⁶ N. Xu, P. Richard, X. Shi, A. van Roekeghem, T. Qian, E. Razzoli, E. Rienks, G.-F. Chen, E. Ieki, K. Nakayama, T. Sato, T. Takahashi, M. Shi, and H. Ding, *Phys. Rev. B* **88**, 220508 (2013).
 - ²⁷ F. Hardy, A. E. Böhmer, L. de' Medici, M. Capone, G. Giovannetti, R. Eder, L. Wang, M. He, T. Wolf, P. Schweiss, R. Heid, A. Herbig, P. Adelmann, R. A. Fisher, and C. Meingast, *Phys. Rev. B* **94**, 205113 (2016).
 - ²⁸ H. Ikeda, R. Arita, and J. Kuneš, *Phys. Rev. B* **81**, 054502 (2010).
 - ²⁹ K. Kuroki, H. Usui, S. Onari, R. Arita, and H. Aoki, *Phys. Rev. B* **79**, 224511 (2009).
 - ³⁰ W. Metzner, M. Salmhofer, C. Honerkamp, V. Meden, and K. Schönhammer, *Rev. Mod. Phys.* **84**, 299 (2012).
 - ³¹ C. Platt, W. Hanke, and R. Thomale, *Adv. Phys.* **62**, 453 (2014).
 - ³² S. Graser, P. J. Hirschfeld, T. Kopp, R. Gutser, B. M. Andersen, and J. Mannhart, *Nature Phys.* **6**, 609 (2010).
 - ³³ S. Graser, A. F. Kemper, T. A. Maier, H.-P. Cheng, P. J. Hirschfeld, and D. J. Scalapino, *Phys. Rev. B* **81**, 214503 (2010).

- (2010).
- ³⁴ T. Miyake, K. Nakamura, R. Arita, and M. Imada, *J. Phys. Soc. Japan* **79**, 044705 (2010).
- ³⁵ C. Platt, R. Thomale, C. Honerkamp, S.-C. Zhang, and W. Hanke, *Phys. Rev. B* **85**, 180502 (2012).
- ³⁶ J. Wang, A. Eberlein, and W. Metzner, *Phys. Rev. B* **89**, 121116 (2014).
- ³⁷ A. F. Kemper, T. A. Maier, S. Graser, H.-P. Cheng, P. J. Hirschfeld, and D. J. Scalapino, *New J. Phys.* **12**, 073030 (2010).
- ³⁸ M. P. Raphael, M. E. Reeves, and E. F. Skelton, *Rev. Sci. Instrum.* **69**, 1451 (1998).
- ³⁹ S. Shatz, A. Shaulov, and Y. Yeshurun, *Phys. Rev. B* **48**, 13871 (1993).
- ⁴⁰ I. I. Mazin, T. P. Devereaux, J. G. Analytis, J.-H. Chu, I. R. Fisher, B. Muschler, and R. Hackl, *Phys. Rev. B* **82**, 180502 (2010).
- ⁴¹ Note that the Fe B_{1g} phonon of the crystallographic (2 Fe) unit cell appears in B_{2g} in the 1 Fe unit cell used here for the analysis of the electronic spectra.
- ⁴² D. Pekker and C. Varma, *Ann. Rev. Cond. Mat. Phys.* **6**, 269 (2015).

Appendix A: Theoretical Methods

1. Model Hamiltonian

To determine the relative strength of s - and d -wave pairing channels in $\text{Ba}_{1-x}\text{K}_x\text{Fe}_2\text{As}_2$ from a model Hamiltonian, the results of which are depicted in Fig. 3 (b) and (c), we start with the five iron d -orbital approach proposed by Graser *et al.*³² for parent BaFe_2As_2 . The tight-binding model,

$$\mathcal{H}_0 = \sum_{\mathbf{k}, s} \sum_{a, b=1}^5 c_{\mathbf{k}as}^\dagger K_{ab}(\mathbf{k}) c_{\mathbf{k}bs}, \quad (\text{A1})$$

with \mathbf{k} , a , s denoting momentum, orbital and spin degrees of freedom, accurately reproduces the *ab initio* band structure of BaFe_2As_2 at low energies³³. The different doping levels are modeled by a rigid band shift, which amounts to 0.1 eV or roughly 2.5% of the bandwidth for $x = 0.5$ potassium substitution. Assuming a pronounced two-dimensional character of the Fermi surface sheets, we restrict the pairing calculation to the 2D cut of the Fermi surface for $k_z = 0$.

For the interaction part \mathcal{H}_{int} , we use a complete set of on-site intra- and interorbital repulsion as well as Hund's and pair-hopping terms,

$$\begin{aligned} \mathcal{H}_{\text{int}} = \sum_i \left[U_{\text{intra}} \sum_a n_{ia\uparrow} n_{ia\downarrow} + U_{\text{inter}} \sum_{a < b, ss'} n_{ias} n_{ibs'} \right. \\ \left. + J_H \sum_{a < b} \vec{S}_{ia} \vec{S}_{ib} + J_{\text{pair}} \sum_{a < b} c_{ia\uparrow}^\dagger c_{ia\downarrow}^\dagger c_{ib\uparrow} c_{ib\downarrow} \right]. \end{aligned} \quad (\text{A2})$$

Both fRG and RPA are independently applied to this microscopic model. The parameter set chosen in fRG is $U_{\text{intra}} = 4.0$ eV, $U_{\text{inter}} = 2.0$ eV and $J_H = J_{\text{pair}} = 0.7$ eV which are close to constrained RPA estimations³⁴. In order to avoid a magnetic instability in RPA, we choose interaction parameters that are smaller than those used in the fRG calculation. We set $U = 0.85$ eV and $U' = U/2$, $J = J' = U/4$. For these parameters, we find that the pairing interaction vertex $V(k, q)$ is determined by spin fluctuations, and orbital fluctuations do not play a significant role. In the fRG, the bare interactions are renormalized to smaller values due to the coupling between the different particle-hole and particle-particle channels. This coupling is absent in the RPA, which is consistent with the need to use smaller bare parameters for the latter.

2. fRG

The method of fRG proved very successful for the prediction and exploration of the interplay between magnetic and superconducting order in iron-based

compounds^{12,31,35}. Its main strength lies in its ability to treat different ordering channels on an equal footing, whilst simultaneously allowing for the study of microscopic models with multiple degrees of freedom. Similar to the familiar fRG concept of thinning out degrees down to a low-energy cutoff Λ which serves as an upper bound for the transition temperature while leaving the low-energy physics invariant^{30,31}, the fRG method provides an effective low-energy theory \mathcal{H}^Λ which immediately (or at least more clearly) reveals the favored ordering tendencies. In this flow to low energies, different fluctuations such as spin and charge density wave, Pomeranchuk, and superconducting ordering tendencies are included on equal footing¹².

Without going into the technical details of the calculations, it is important to mention that one usually implements the fRG in terms of an appropriate band basis γ_k^\dagger , γ_k which diagonalizes the quadratic part Eq. (A1). The effective low-energy description in this basis then reads

$$\mathcal{H}^\Lambda = \mathcal{H}_0^\Lambda + \sum_{k_1, \dots, k_4} \tilde{V}^\Lambda(k_1, k_2, k_3, k_4) \gamma_{k_1}^\dagger \gamma_{k_2}^\dagger \gamma_{k_3} \gamma_{k_4}, \quad (\text{A3})$$

with a renormalized quadratic part \mathcal{H}_0^Λ and an effective two-particle interaction \tilde{V}^Λ . In the fRG flow, spontaneous symmetry breaking is signalled by diverging effective interactions at a critical energy scale Λ_c . In the "standard" fRG, the 2-particle vertex \tilde{V}^Λ is computed from an fRG flow (integrated) down to a "mean-field" scale Λ_{MF} slightly above the critical scale Λ_c . This first part of our calculation is similar to our earlier study of hole-doped $\text{Ba}_{1-x}\text{K}_x\text{Fe}_2\text{As}_2$ ¹², where further details can be found.

However, to compare the fRG leading eigenvalues in the s_{\pm} - and d -channels with experiment and with the RPA results, based on the eigenvalue description of the dominant and subdominant Raman peaks, we have to "roll back" this particle-particle-channel to obtain the *pp-irreducible pairing interaction*. This is discussed in Ref. 36 with application to the single band Hubbard model. It amounts to solving a linear integral (Bethe-Salpeter) equation for the pp-irreducible vertex $V(k, q)$, where $V(k, k') \equiv V(k, k', k', k)$, i.e.

$$\tilde{V}^\Lambda(k, q) = V^\Lambda(k, q) - \int_p V^\Lambda(k, p) G^\Lambda(p) G^\Lambda(-p) \tilde{V}^\Lambda(p, q), \quad (\text{A4})$$

schematically shown in Fig. 4 below. Here $\tilde{V}^\Lambda(k, q)$ denotes the usual (1-particle irreducible) vertex obtained from the "standard" fRG, including all modes down to Λ_{MF} , which is chosen slightly above the critical scale Λ_c : the explicit solution is obtained as $V^\Lambda = \tilde{V}^\Lambda(1 - D^\Lambda \tilde{V}^\Lambda)^{-1}$, i.e. matrix inversion, due to the usual discretization of momentum space in patches rendering the kernel of Eq. (A4) separable. This kernel, or diagonal matrix, D is radially integrated in each patch with the frequency sum in Eq. (A1) evaluated analytically.

This pp-irreducible fRG vertex is inserted in Eq. (1) to obtain the eigenvalue decomposition λ_α , where λ_2/λ_1

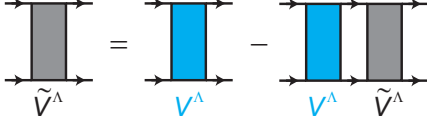


FIG. 4. Diagrammatic relation between V^Λ and \tilde{V}^Λ . Fermionic propagators are illustrated by solid black lines, the interactions V^Λ and \tilde{V}^Λ by blue and grey boxes, respectively.

as well as λ_3/λ_1 is then compared against RPA and the experimental finding as described in the main text. (The integral measure in Eq. (1) becomes $\int_{\text{FS}} dq \equiv \sum_i \int_{\text{FS}_i} d^2q/2\pi v_F(q)$, where the index i runs over all Fermi surface pockets and $v_F(q)$ denotes the Fermi velocity.)

Choosing the pp-irreducible vertex within the fRG approach also substantially reduces the quantitative influence of the fRG-cutoff Λ_{MF} : by rolling back the pp-channel to V (Fig. 4), one takes out a steeply growing logarithm. This can be most easily seen if the kernel D is assumed to be a constant d . In this case, V^Λ and \tilde{V}^Λ would have the eigenvalues related by $\lambda = \frac{\tilde{\lambda}}{1-d\lambda}$. The reduction of the cutoff influence, provided the particle-hole correlations, i.e. spin-fluctuations, die out at low enough scales, then holds, and hence the pp-irreducible pairing interaction has saturated at Λ_{MF} .

For K substitution larger than $x \approx 0.25$, the pairing fluctuations with the effective (renormalized) two-particle irreducible interactions $V_{\text{fRG}}^\Lambda(k, -k, q, -q) \equiv V^\Lambda(k, q)$ [Eqs. (A3) and (A4)] are dominant in the low-energy regime, which justifies us to constrain ourselves to the Cooper channel and hence superconducting Fermi surface instabilities.

3. RPA

In the RPA approximation, the pair structure which arises from a spin-fluctuation exchange interaction is determined from the scattering vertex

$$\Gamma_{ij}(\mathbf{k}, \mathbf{k}') = \text{Re} \sum_{\ell_1 \ell_2 \ell_3 \ell_4} a_{\nu_i}^{\ell_1, *}(k) a_{\nu_i}^{\ell_4, *}(k) \times \Gamma_{\ell_1 \ell_2 \ell_3 \ell_4}(\mathbf{k}, \mathbf{k}', \omega = 0) a_{\nu_j}^{\ell_2}(k') a_{\nu_j}^{\ell_3}(k'). \quad (\text{A5})$$

Here the momenta \mathbf{k} and \mathbf{k}' are restricted to the Fermi surface $\mathbf{k} \in \mathcal{C}_i$ and $\mathbf{k}' \in \mathcal{C}_j$ where i and j label the different pockets, and $a_\nu^\ell(\mathbf{k})$ are the orbital components of the band eigenvectors. The particle-particle scattering vertex between orbitals ℓ_1, ℓ_4 and ℓ_2, ℓ_3 is given by

$$\Gamma_{\ell_1 \ell_2 \ell_3 \ell_4}(\mathbf{k}, \mathbf{k}', \omega) = \left[\frac{3}{2} \bar{U}^s \chi_s^{\text{RPA}}(\mathbf{k} - \mathbf{k}', \omega) \bar{U}^s + \frac{1}{2} \bar{U}^s (\text{A6}) - \frac{1}{2} \bar{U}^c \chi_c^{\text{RPA}}(\mathbf{k} - \mathbf{k}', \omega) \bar{U}^c + \frac{1}{2} \bar{U}^c \right].$$

The interaction matrices in orbital space for spin and charge channels, \bar{U}^s and \bar{U}^c respectively, contain linear

combinations of the interaction parameters U, U', J and J' (see e.g. Ref. 37). The RPA spin- (χ_s^{RPA}) and charge (χ_c^{RPA}) susceptibilities have the usual form

$$\chi_{c/s, \ell_1 \ell_2 \ell_3 \ell_4}^{\text{RPA}}(\mathbf{q}) = \left\{ \chi^0(\mathbf{q}) [1 \pm \bar{U}^{c/s} \chi^0(\mathbf{q})]^{-1} \right\}_{\ell_1 \ell_2 \ell_3 \ell_4} \quad (\text{A7})$$

with the bare susceptibility matrix

$$\chi_{\ell_1 \ell_2 \ell_3 \ell_4}^0(\mathbf{q}, \omega) = -\frac{1}{N} \sum_{\mathbf{k}, \mu\nu} a_\nu^{\ell_4}(\mathbf{k}) a_{\nu'}^{\ell_2, *}(k) a_\mu^{\ell_1}(\mathbf{k} + \mathbf{q}) a_{\mu'}^{\ell_3, *}(k + \mathbf{q}) \times \frac{f(E_\nu(\mathbf{k})) - f(E_\mu(\mathbf{k} + \mathbf{q}))}{\omega + i0^+ + E_\nu(\mathbf{k}) - E_\mu(\mathbf{k} + \mathbf{q})}. \quad (\text{A8})$$

Here, $f(E)$ is the Fermi function and $E_\nu(\mathbf{k})$ is the energy dispersion for band ν . The symmetry function $g(\mathbf{k})$ of the pairing state can then be found by solving an eigenvalue problem of the form

$$-\sum_j \oint_{\mathcal{C}_j} \frac{d\mathbf{k}'_{\parallel}}{2\pi v_F(\mathbf{k}'_{\parallel})} \Gamma_{ij}(\mathbf{k}, \mathbf{k}') g_\alpha(\mathbf{k}') = \lambda_\alpha g_\alpha(\mathbf{k}), \quad (\text{A9})$$

where $v_F(\mathbf{k})$ is the Fermi velocity. The eigenfunction $g_\alpha(\mathbf{k})$ with the largest eigenvalue λ_α gives the leading instability (ground state) of the system and sub-leading instabilities have smaller λ_α . We have executed all steps within the RPA formalism once again to illustrate the precise form equivalence between Eq. (A9) and Eq. (1) in the main text upon the identification $\int_{\text{FS}} \equiv \sum_j \oint_{\mathcal{C}_j} \frac{d\mathbf{k}'_{\parallel}}{2\pi v_F(\mathbf{k}'_{\parallel})}$ as well as $V(k, q) \equiv \Gamma_{ij}(\mathbf{k}, \mathbf{k}')$.

Appendix B: Samples

The single crystals of hole doped $\text{Ba}_{1-x}\text{K}_x\text{Fe}_2\text{As}_2$ were grown using a self-flux technique and have been characterized elsewhere^{22,23}. The potassium concentration was determined by microprobe analysis. For all samples studied we measured the non-linear magnetic susceptibility $\chi_m^{(3)}(T)$. The results are compiled in Fig. 5. $\chi_m^{(3)}(T)$ is particularly sensitive to inhomogeneities of the samples³⁸. The susceptibility was measured during a continuous warm up (+)/cool down (-) at a rate of typically ± 2 K per minute. According to Shatz and coworkers³⁹, $T_{c\pm}$ is the extrapolation of the linear part to zero voltage at three times the excitation frequency $3f$ with $f = 33$ kHz. We define $T_c = 0.5(T_{c+} + T_{c-})$. The tail above $T_{c\pm}$ is a reliable estimate of the transition width ΔT_c . For the Raman measurements samples with narrow superconducting transitions were selected having ΔT_c values in the range 0.4 to 2 K. The doping levels and typical sample temperatures are displayed in Fig. 1(a). The parameters are compiled in Table I.

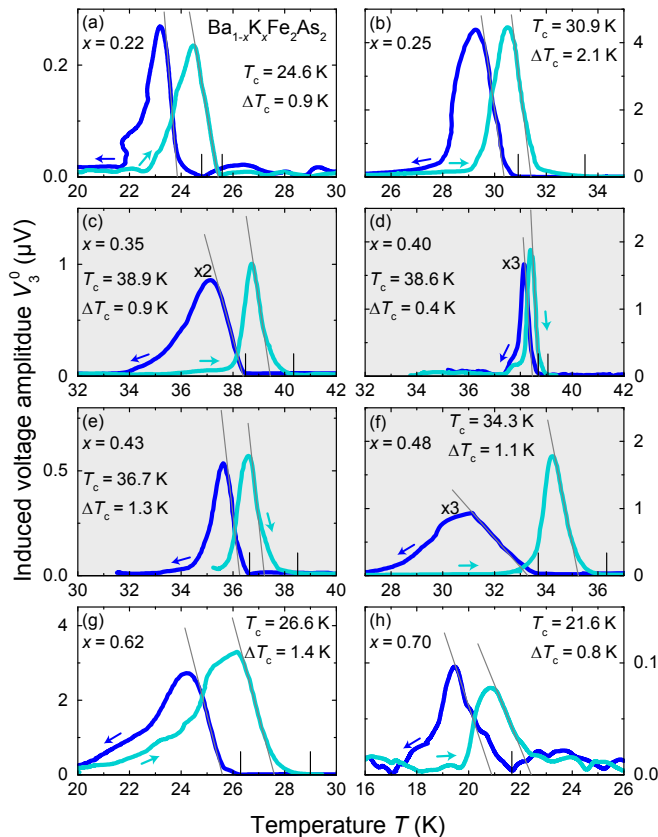


FIG. 5. Non-linear susceptibility of all samples measured. The two data sets correspond to warm up (turquoise) and cool down (blue). $T_{c\pm}$ is the extrapolation of the linear part to zero voltage, the tail above $T_{c\pm}$ corresponds to the transition width ΔT_c ³⁹.

TABLE I. Parameters of the $\text{Ba}_{1-x}\text{K}_x\text{Fe}_2\text{As}_2$ samples studied. The doping levels of the samples used for the quantitative analysis are shown in bold face. Samples labeled with a and b were prepared in the laboratories of H.-H. Wen²² and T. Wolf²³, respectively.

K doping x	T_c (K)	ΔT_c (K)	source
0.22	24.6	0.9	b
0.25	30.9	2.1	a
0.35	38.9	0.9	b
0.40	38.6	0.4	a
0.43	36.7	1.3	b
0.48	34.3	1.1	b
0.62	26.6	1.4	b
0.70	21.6	0.8	b

Appendix C: Experiment

The experiments were performed with standard light scattering equipment. For excitation a solid state laser (Coherent, Genesis MXSLM) was used emitting at 575 nm. The samples were mounted on the cold finger

of a He-flow cryostat in a cryogenically pumped vacuum. The laser-induced heating was determined experimentally to be close to 1 K per mW absorbed laser power. Spectra were measured in the four polarization configurations xy , $x'y'$, RR , and RL where x and y are along the Fe-Fe bonds, $x' = 1/\sqrt{2}(x + y)$, $y' = 1/\sqrt{2}(y - x)$, and $R/L = 1/\sqrt{2}(x \pm iy)$. All symmetry components (A_{1g} , A_{2g} , B_{1g} , and B_{2g} for tetragonal $\text{Ba}_{1-x}\text{K}_x\text{Fe}_2\text{As}_2$) can be extracted using linear combinations of the experimental spectra. For the symmetry assignment we use the 1Fe per unit cell [cf. Fig. 1(b) for the corresponding BZ]^{17,40}. The spectra we show within this work represent the response $R\chi''(\Omega, T)$ which is obtained by dividing the cross section by the Bose-Einstein factor $\{1 + n(T, \Omega)\} = [1 - \exp(-\hbar\Omega/k_B T)]^{-1}$ in which R is an experimental constant. In some cases we isolate superconductivity-induced contributions by subtracting the response measured at $T \gtrsim T_c$ from the spectra taken at $T \ll T_c$ and label the difference spectra $\Delta R\chi''(\Omega, T)$.

Appendix D: Resonance effects

Figure 6 shows the difference spectra $\Delta R\chi''(\Omega) = R\chi''(\Omega, T = 10 \text{ K}) - R\chi''(\Omega, T \gtrsim T_c)$ of the Raman response for excitation lines at 458, 514, 532, and 575 nm. For non-resonant scattering processes one would expect the response to be independent of the excitation. This worked well for optimally doped $\text{Ba}(\text{Fe}_{0.939}\text{Co}_{0.061})_2\text{As}_2$ ⁴⁰. Here, we observe little changes upon switching between green and yellow excitation in A_{1g} and B_{2g} symmetry [Fig. 6(a) and (b)]. In B_{1g} symmetry [Fig. 6(c)], the overall intensity reduces for 532 nm with respect to 575 nm excitation wave length, whereas a substantial enhancement of spectral weight is found for 514 and 458 nm. In the latter case both the pair-breaking peak and the BS mode shift. At first glance, this indicates a dependence on the details of the experiment. However, the BS mode does not change shape and by and large follows the intensity of the pair-breaking peaks. The change of the pair breaking effect for 458 nm indicates the appearance of an orbital-dependent resonance. In the blue the enhancement occurs on those parts of the Fermi surface which have a larger gap. As a consequence, the collective mode which is directly derived from the pair breaking intensity shifts accordingly. Qualitatively, this is further support for the collective character of the mode at 140 cm^{-1} although the details need to be worked out in a future systematic study. Resonance effects must be considered for blue photons, but are weak for yellow photons and hence do not interfere with the analysis of this work.

Appendix E: Symmetry-resolved spectra

Figure 7 shows the raw data in the three main polarization configurations xx , $x'y'$ and RR measured for

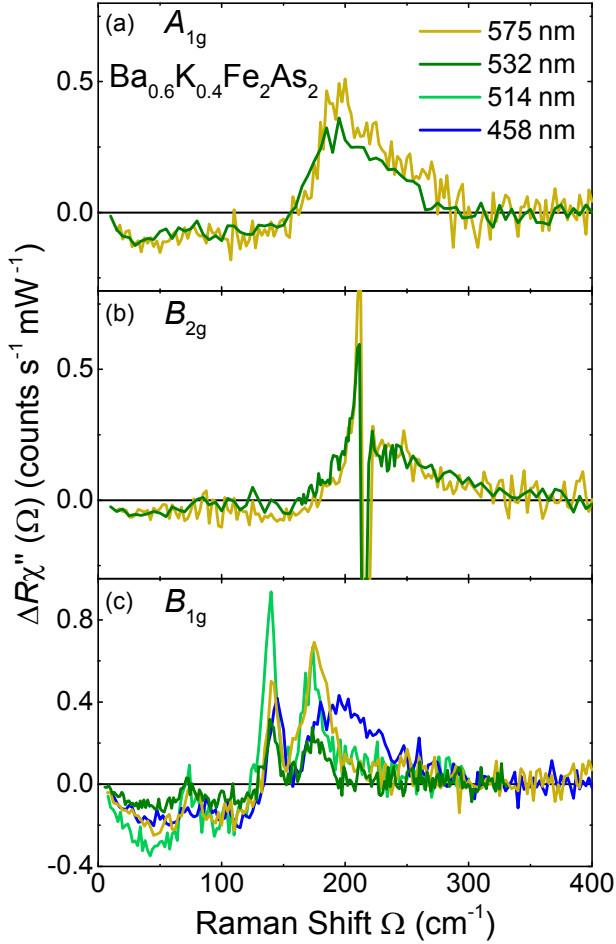


FIG. 6. Resonance effects in $\text{Ba}_{1-x}\text{K}_x\text{Fe}_2\text{As}_2$ at $x = 0.40$. Shown are the difference spectra $\Delta R\chi''(\Omega) = R\chi''(\Omega, T = 10 \text{ K}) - R\chi''(\Omega, T \gtrsim T_c)$ for the three Raman-active symmetries (see text and Fig. 2). The spectra are measured with the laser lines at 575, 532, and 458 nm (only B_{1g}).

this study at temperatures indicated in Fig. 1. The $x'y'$ normal-state spectra at $x = 0.35$ are multiplied by 0.84 to make them match the superconducting spectra. The superposed narrow lines in B_{2g} and A_{1g} symmetry are Raman-active phonons⁴¹.

For a few samples we also measured spectra at intermediate temperatures which are partially published⁵. For deriving the symmetry-resolved spectra also the RL configuration is needed. The full symmetry analysis is available for $0.35 \leq x \leq 0.70$ as shown in Fig. 8. The A_{2g} spectra are temperature independent and typically on order 10% of those of the other symmetries. They vanish for $x = 0.7$. Therefore, for avoiding subtraction procedures, reducing the time for the measurements and improving the statistics we can use the spectra measured at $xx, x'y'$ and RR (Fig. 7).

Except for the spectra at $x = 0.22$ and 0.25 there are pair-breaking features in all symmetries (except for A_{2g}). In general, the structures are narrower and more

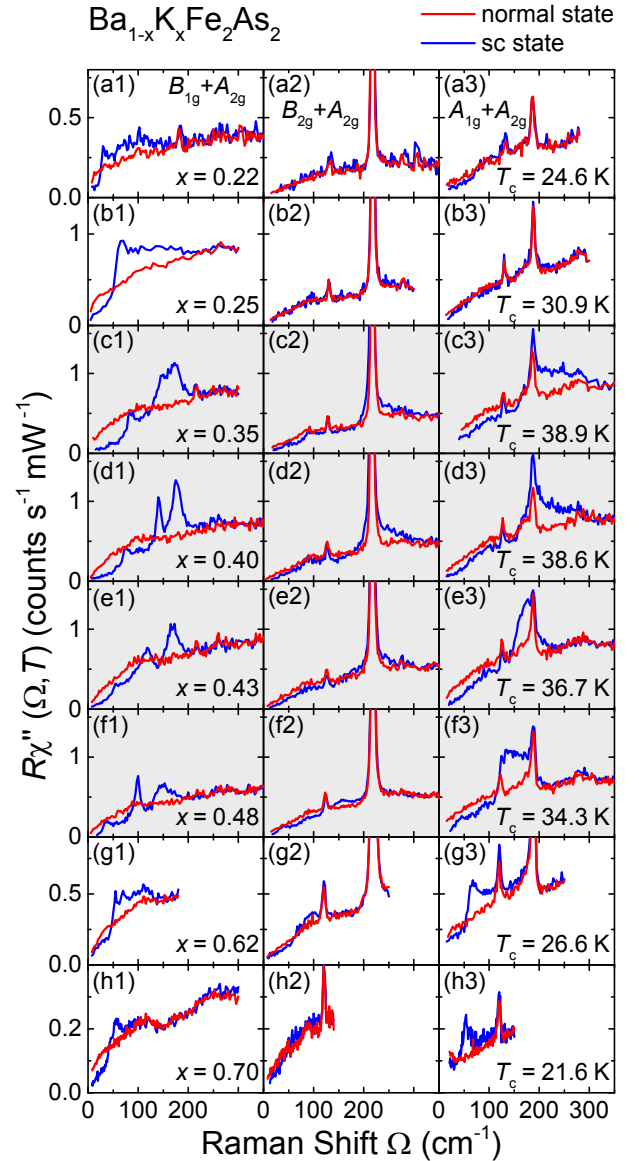


FIG. 7. Doping-dependent Raman spectra. The Raman response $R\chi''(\Omega, T, x)$ (raw data after division by the Bose-Einstein factor) of $\text{Ba}_{1-x}\text{K}_x\text{Fe}_2\text{As}_2$ is shown in $x'y'$ ($B_{1g} + A_{2g}$), xy ($B_{2g} + A_{2g}$), and RR ($A_{1g} + A_{2g}$) polarization above (red) and below (blue) T_c . The results around optimal doping, $0.35 \leq x \leq 0.48$, are highlighted.

pronounced in B_{1g} than in A_{1g} and B_{2g} symmetry (see also Fig. 8). The B_{1g} spectra at $x = 0.22, 0.25, 0.62,$ and 0.70 [Fig. 7 (a1), (b1), (g1), (h1)] are qualitatively different from those around optimal doping [Fig. 7 (c1), (d1), (e1), (f1)]. Whereas a narrow mode or an indication thereof is still found along with an isolated broad maximum for $x = 0.62$ and $x = 0.70$, respectively, there are only broad maxima at 30 cm^{-1} and 65 cm^{-1} next to shoulders around 100 and 150 cm^{-1} for $x = 0.22$ and 0.25 , respectively.

Figure 9 shows the entire set of difference spectra in B_{1g} symmetry. Away from optimal doping the experi-

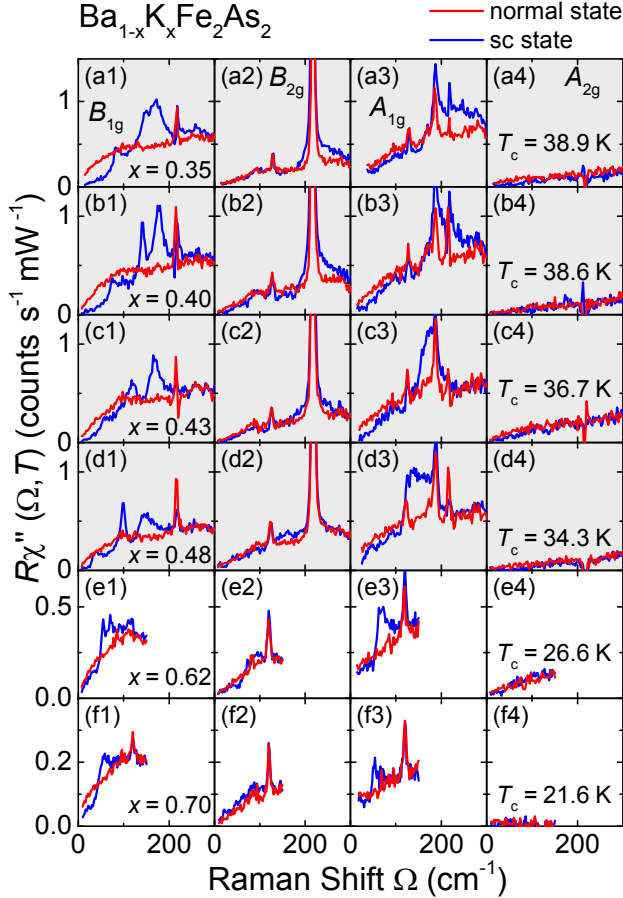


FIG. 8. Symmetry-resolved spectra of $\text{Ba}_{1-x}\text{K}_x\text{Fe}_2\text{As}_2$. The spectra for doping levels x as indicated are measured at approximately 8 K (blue) and above (red) the respective transition temperatures. The contributions from A_{2g} symmetry are structureless, temperature independent, and substantially smaller than those in the other symmetries.

ments become more difficult to analyze. At $x = 0.62$ there are still three superconductivity-induced structures at low temperature similar to those around optimal doping. The low-energy peak is very weak at $x = 0.62$ (open green arrow), if existent at all, and is definitely unobservable at $x = 0.70$. We believe that it is related to the lower BS mode but find it difficult to furnish experimental proof for this hypothesis.

At $x = 0.22$ and 0.25 $\Delta\chi''(\Omega, T)$ vanishes only at $10 k_B T_c$. Consequently, the shoulders developing in the energy range around $100\text{--}150\text{ cm}^{-1}$ ($4\text{--}10 k_B T_c$; open blue arrows in Fig. 2) are likely to have a relationship to the spin density wave (SDW). Then, the prominent maxima at 30 and 65 cm^{-1} ($3 k_B T_c$), which show little or no temperature dependence [for $x = 0.25$ see supplemental Fig. 7 (b1–b3)] similar to the pair-breaking peaks studied at optimal doping $x = 0.40^5$, are probably gap excitations on the outer hole band which is less affected by the SDW forming below approximately 80 K. Very speculatively one could also interpret them in terms of fluctu-

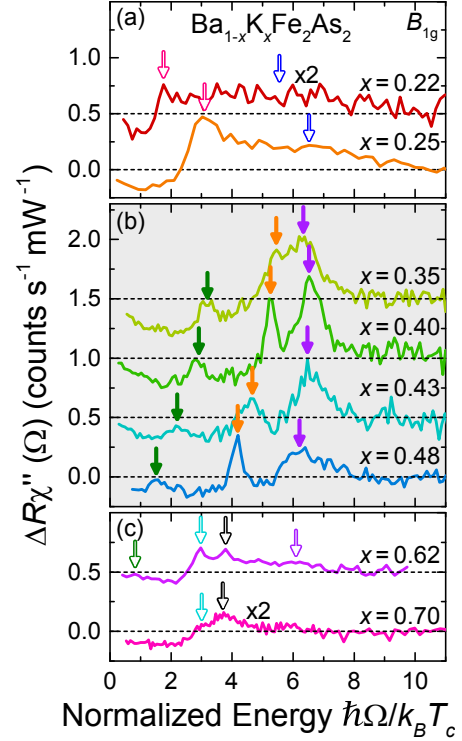


FIG. 9. Difference spectra $\Delta R\chi''(\Omega, x)$ in B_{1g} symmetry. The energy scale is normalized to the respective T_c values of the differently doped samples. The intensities are off-set, the dashed horizontal lines mark zero. The purple arrows indicate the pair-breaking features at high energy. Orange and green arrows mark the BS modes pulled off of the energy gap. The open black arrow indicates the additional maxima observed at $x = 0.62$ and 0.70 . Open symbols indicate features with tentative assignment.

ations of the superconducting order parameter (“Higgs modes”) activated by the presence of the SDW⁴². The other bands are expected to participate in the SDW formation as they are better nested and are likely to be gapped out at least partially already above T_c .

Appendix F: Symmetry dependence for $0.35 \leq x \leq 0.48$

In Fig. 10 we show the difference spectra for the doping range around $x = 0.40$. For all doping levels around optimal doping a pronounced narrow mode below 100 cm^{-1} exists only in B_{1g} symmetry. In the other symmetries there are only broad shoulders at slightly different energies or no structures at all. For this reason, the mode cannot be a signature of the small gap on the outer hole band which would appear also in the A_{1g} and possibly in the B_{2g} spectra.

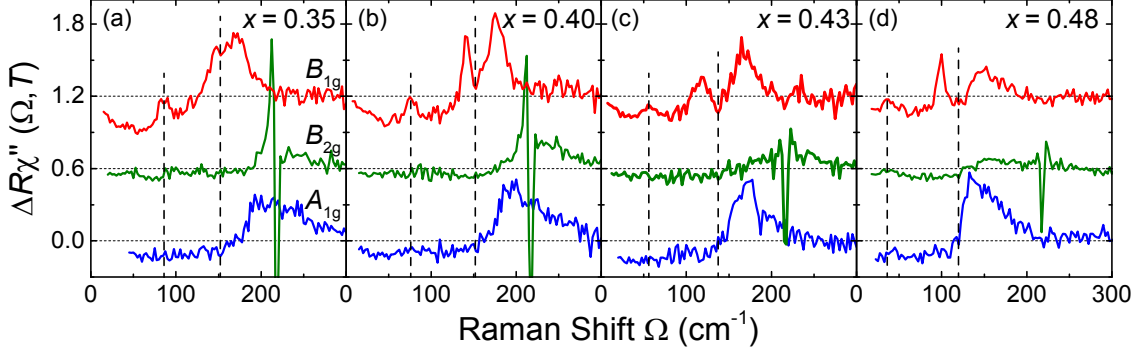


FIG. 10. Difference spectra $\Delta R\chi''(\Omega, x)$ for all symmetries close to optimal doping. The dashed vertical lines are intended to demonstrate the uniqueness of the low-energy B_{1g} peak.

Appendix G: Pair breaking and final-state interaction

In addition to the usual pair-breaking features close to the gap energy 2Δ $\text{Ba}_{1-x}\text{K}_x\text{Fe}_2\text{As}_2$ has two narrow modes inside the gap which originate from the interaction between the electrons of the broken pair as described first by Bardasis and Schrieffer³. For demonstrating the final state interaction to be important the spectra were compared to a phenomenological prediction as described in detail in Ref. 5. In brief, the band-dependent gap values are derived from the spectra in B_{2g} and A_{1g} symmetry determining also the bare B_{1g} spectra. Then, the final-state interaction between the electrons of a broken pair is cranked up until the experimental B_{1g} spectra can be reproduced. The closer the coupling λ_d in the subdominant d -wave channel approaches that in the dominant pairing channel λ_s the larger the binding energy E_b of the exciton-like state. Here, E_b means the difference between the gap edge and the position of the collective mode Ω_{BS} . The results of a full 3D phenomenological description are shown in Fig. 13 for the weaker $d(2)$ -wave channel BS(2) and doping levels $0.35 \leq x \leq 0.48$.

For the full 3D calculation we use a phenomenological eigenvector $g(\mathbf{k})$ since the fRG and RPA results for $g(\mathbf{k})$ exist only for $k_z = 0$. The relative coupling strength λ_d/λ_s increases monotonically with doping, as plotted in Fig. 3. The values used for the gaps are compiled in Table II. The phenomenology shows also that the gap on the outer hole band can indeed be observed in all symmetries in the range below 80 cm^{-1} but the predicted intensity of the pair-breaking maximum in B_{1g} symmetry is at least an order of magnitude too weak to explain the experiment (Fig. 13).

This discrepancy inspired us to search for an alternative explanation in terms of a second BS mode as described in Ref. 19. Since the eigenvectors of the two $d(i)$ -wave channels are orthogonal the BS mode for the stronger subleading channel BS(2) can be fitted independently [Fig. 13 (e)]. Here the model function is calculated

only in 2D since we know the eigenvectors only for $k_z = 0$. By using the bare 2D eigenvectors of the subleading channels the fits around 2Δ become worse than in the case and the full analysis. We will address this problem in an upcoming publication.

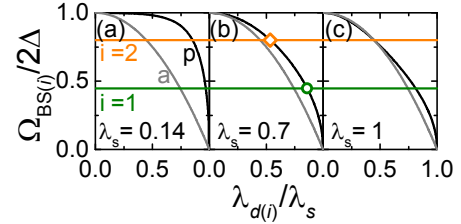


FIG. 11. Determination of the relative coupling strengths. The relation between the positions of the BS modes and the ratio of the coupling strength $\lambda_{d(i)}/\lambda_s$ for $x = 0.4$ is shown. The horizontal green and orange lines represent the positions of the BS(1) and BS(2) modes, respectively. The curves show the numerically determined relations between the $E_{b(i)}/2\Delta$ and $\lambda_{d(i)}/\lambda_s$ for λ_s as indicated. The limiting case (see text) $\lambda_z = 0$ (black) is shown along with the approximation $\sqrt{E_{b(i)}/2\Delta} = \lambda_{d(i)}/\lambda_s$ (grey). For our analysis we used $\lambda_s = 0.7$ and $\lambda_z = 0$ (green circle and orange diamond in (b)).

The ratio $\lambda_{d(i)}/\lambda_s$ in the fits¹³ and in the single-band results of Monien and Zawadowski⁴ depends on λ_s . We use $\lambda_s = 0.7$ as an approximation inspired by the Eliashberg analysis in Refs. 28 and 29.

We cannot derive the absolute magnitude of λ_s from our experiments. However, we use the experimental positions of the two BS modes and determine $\lambda_{d(1)}$ and $\lambda_{d(2)}$ for three different values of λ_s as shown for $x = 0.4$ in Fig. 11. We evaluated the limiting case of $\lambda_z = 0$ (black) where λ_z is the coupling in the particle-hole channel. For $\lambda_s \simeq 1$, $\sqrt{E_b}/2\Delta = \lambda_d/\lambda_s$ (grey) is a useful approximation^{5,14} independent of λ_z . The best agreement between $\lambda_{d(i)}/\lambda_s$ and the ratio derived from fRG and RPA is found for $0.7 \leq \lambda_s \leq 1$ in agreement with the Eliashberg result^{28,29}. For obtaining the numerical

TABLE II. Parameters of the phenomenological fits. We compile the fitting parameters for the phenomenological fits applied to the B_{1g} results of $\text{Ba}_{1-x}\text{K}_x\text{Fe}_2\text{As}_2$ at doping levels as indicated. All energies are given in units of cm^{-1} . According to Ref. 5 the pockets are labeled as h1 (inner hole pocket), h2 (middle hole pocket), h3 (outer hole pocket), e1 (outer electron pocket), and e2 (inner electron pocket).

x	$\Delta_{\min}^{\text{h1}}$	$\Delta_{\max}^{\text{h1}}$	$\Delta_{\min}^{\text{h2}}$	$\Delta_{\max}^{\text{h2}}$	$\Delta_{\min}^{\text{h3}}$	$\Delta_{\max}^{\text{h3}}$	$\Delta_{\min}^{\text{e1}}$	$\Delta_{\max}^{\text{e1}}$	$\Delta_{\min}^{\text{e2}}$	$\Delta_{\max}^{\text{e2}}$	Ω_{BS}
0.35	180	195	150	256	80	90	165	212	180	210	148
0.40	155	197	170	258	68	80	171	211	177	186	141
0.43	148	162	150	250	50	58	158	210	160	172	119
0.48	123	135	135	150	32	38	138	161	123	133	100

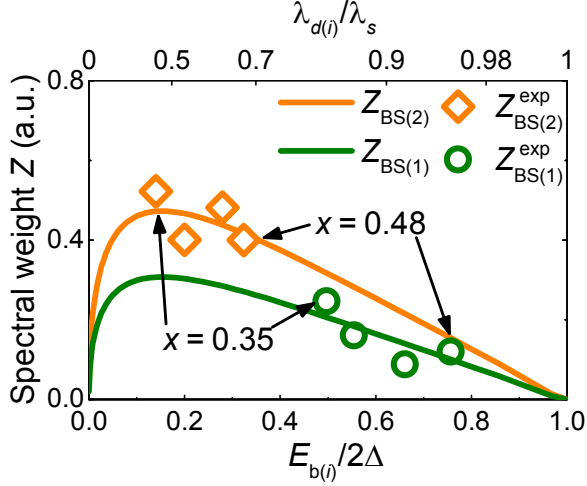


FIG. 12. Intensities of the collective modes. The intensities of BS(1) and BS(2) are shown as a function of the relative coupling strength $\lambda_{d(i)}/\lambda_s$ ($i = 1, 2$; $\lambda_s = 0.7$) for the two sub-leading channels). The orange diamonds and green circles represent the experimentally obtained spectral weights of the strong- ($E_{b(1)} \simeq 2\Delta$) and weak-coupling ($E_{b(2)} \ll 2\Delta$) BS modes, respectively. The solid orange and green lines indicate the theoretically expected integrated spectral weight in the BS mode, with $Z_{BS(1)} = 0.65Z_{BS(2)}$.

value we set $\lambda_z = 0$. Naïvely one would expect the spectral weight in the BS modes $Z_{BS(i)}$ to increase continuously along with $E_{b(i)}/2\Delta$ or, in a different way, with $\lambda_{d(i)}/\lambda_s$. However, $Z_{BS(i)}$ has a maximum already at small $\lambda_{d(i)}/\lambda_s$ as the position of the pole itself depends on the ratio $E_{b(i)}/2\Delta$ or $\lambda_{d(i)}/\lambda_s$ ^{4,13}. For this reason the BS mode corresponding to the stronger $d(1)$ channel ($E_{b(1)} \simeq 2\Delta$) has a weaker intensity than the other one ($E_{b(2)} \ll 2\Delta$). In Fig. 12 we show $Z_{BS(i)}$ of the two BS modes for $0.35 \leq x \leq 0.48$. The experimental values for $Z_{BS(1)}$ and $Z_{BS(2)}$ are adjusted to the theory curves using the same factor. The theoretical curves for BS(1) and BS(2) are different because of the different eigenvectors $g_{d(1)}(\mathbf{k})$ and $g_{d(2)}(\mathbf{k})$. Since $g_{d(1)}(\mathbf{k})$ has more nodes the Fermi surface integral is smaller than for $g_{d(2)}(\mathbf{k})$.

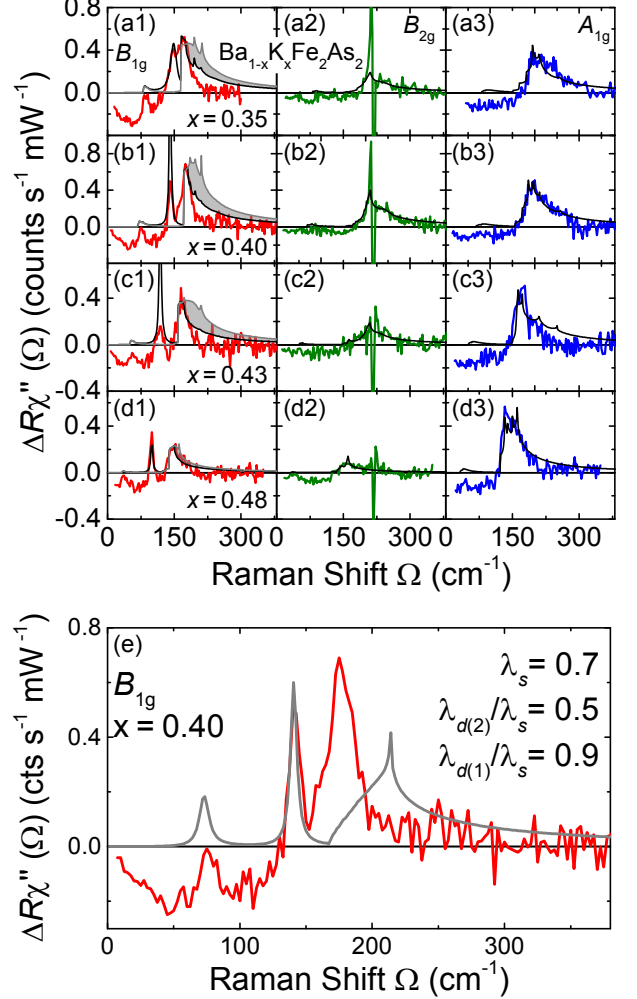


FIG. 13. Difference spectra and 3D phenomenological fits. The fits are applied to the data as described in detail in Ref. 5. (a1 - d1) The grey-shaded area indicates the spectral weight that is transferred from the pair-breaking peak into the collective mode. (e) 2D model fit with two BS modes. Also here $\lambda_s = 0.7$ is used yielding ratios of $\lambda_{d(1)}/\lambda_s = 0.9$ and $\lambda_{d(2)}/\lambda_s = 0.5$.